Toward Parametrization of Precipitating Shallow Cumulus Cloud Organization via Moisture Variance

Marius Levin Thomas[1,2] , **Ivan Bašták Ďurán[1]** , **and Juerg Schmidli[1]**

[1]Institute for Atmospheric and Environmental Sciences, Goethe-University, Frankfurt am Main, Germany, [2]Institute for Atmospheric Physics, Johannes Gutenberg University, Mainz, Germany

Abstract The influence of the initial vertical moisture profile on precipitating shallow cumulus cloud organization in terms of the column-averaged moisture variance is investigated using large-eddy simulations. Five idealized simulations based on the Rain in Cumulus over the Ocean field experiment with different initial moisture profiles are investigated. All cases simulate precipitating shallow cumulus convection in a marine sub-tropical region under large-scale subsidence. The results show that the moisture variance is mainly generated through the interaction of the moisture flux and the moisture gradient in the gradient production term at the top of the boundary layer. The development is characterized by three regimes: initial, transition, and quasi-steady regime. During the initial regime, the moisture gradient is built up by moisture accumulation until precipitating convection starts. Within the transition regime, precipitation enables mesoscale cloud organization with enhanced convective activity and moisture fluxes. The moisture variance increases from the moist to the dry initial moisture profiles. In a following quasi-steady regime, the moisture variance is approximately preserved. Thereby, the initial moisture gradient between the average sub-cloud layer and the free atmosphere is found to be an important factor for the generation of the quasi-steady column-averaged moisture variance. The result suggests that a resolved-scale variable like the moisture gradient can be used to estimate the quasi-steady state conditions resulting from cloud organization. This finding may serve as a starting point for the parametrization of the subgrid scale cloud organization caused by precipitating shallow convection.

1. Introduction

Modeling of shallow convection clouds is a source of uncertainty in current weather prediction and climate models (Bony & Dufresne, 2005; Bony et al., 2015; Sherwood et al., 2014; Webb et al., 2006). Because shallow cumulus clouds are almost omnipresent and modify the radiative energy budget, this has a significant influence on the skill of the models. A possible reason for this shortcoming is the inaccurate representation of the effects of precipitation in shallow convection (e.g., Rauber et al., 2007).

Precipitation is important, because with its formation shallow cumulus clouds can organize from randomly distributed fields into mesoscale patterns, for example, cloud clusters or mesoscale arcs (Nair et al., 1998; Seifert & Heus, 2013; Snodgrass et al., 2009). These cloud structures enable self-aggregation via feedbacks between internal cloud dynamics and external forcing factors. Cloud organization modifies complex interactions among physical processes within the cloud-topped boundary layer and changes properties of the thermodynamic environment (Anurose et al., 2020).

More specifically, the vertical transport of moisture in moist convective updrafts creates localized moisture anomalies in the upper part of the atmospheric boundary layer (ABL) during cloud formation. When precipitation evaporates below the cloud base, additional moisture anomalies are induced by the formation of cold pools (Zuidema et al., 2012). This triggers further convection by latent heat release and/or the dynamics at the boundaries of propagating density currents and thus promotes cloud organization (Anurose et al., 2020; Seifert & Heus, 2013).

From the modeling perspective, most turbulence and convection parametrizations do not consider precipitation from shallow cumulus clouds and also do not account for the associated cloud organization. Since precipitation and cloud organization can significantly alter the mean properties of the ABL, the lack of their representation can have a strong impact (Vial et al., 2017). Therefore, it is important to introduce the effect of cloud organization into the parametrization of shallow convection.

In order to parameterize cloud organization, a quantification of this process is required. Cloud organization can be quantified via indices based on feature detection (see, e.g., Tobin et al., 2012; Tompkins & Semie, 2017), but this approach is very difficult to use in a parameterization since it requires detailed information about subgrid scale horizontal distribution. Higher order moments, particularly the moisture variance, already contain such information in a compact way (see Anurose et al., 2020, for more details), thus they can be used as a relatively simple quantification of organization. It has been shown by multiple authors (Anurose et al., 2020; Bretherton & Blossey, 2017; Griffin & Larson, 2016; Schemann & Seifert, 2017; Seifert & Heus, 2013), that cloud organization often coincides with an increase in the moisture variance, especially for cases with precipitation. A detailed investigation of Anurose et al. (2020) indicates that the moisture variance is significantly increased during cloud organization, when the convective activity is intensified. The main source in the generation of the variance is the interaction of the moisture flux with the moisture gradient in the gradient production term. According to Anurose et al. (2020), the temporal evolution of the moisture variance can be divided into three regimes. In the initial regime, moisture variance increases only marginally and the surface moisture flux leads to an accumulation of moisture within the boundary layer up to a certain threshold. In the following transition regime, large amounts of moisture variance are generated by the penetration of convection through the top of the ABL. This process continues until a quasi-steady regime is reached, where the generation of moisture variance is balanced by the remaining terms in the budget equation. Anurose et al. (2020) showed that until the quasi-steady regime is reached, the gained moisture variance is greater for a dry initial moisture profile than for a moister one.

The understanding of the quasi-steady regime can be useful for the parametrization of cloud organization. Equilibrium states are often used as a building stone in the design of a parametrization, as for example, in moist convection schemes based on the mass-flux approach (e.g., Fritsch & Chappell, 1980; Tiedtke, 1989) or in TKE turbulence schemes (e.g., Ďurán et al., 2018). They are taken as a reference, to which the model should converge, or the parametrization attempts to quantify the fluctuations of the model state from the equilibrium state. The quasi-steady regime resulting from the organization of shallow convection can be expressed to some degree by a quasi-steady state of moisture variance. As indicated by Anurose et al. (2020), the moisture variance seems to depend on the initial profile of moisture, but that study was based on only two cases. We will analyze five cases (see below) with different initial profiles of moisture. This larger data set is more suitable to determine whether the initial profiles of moisture have a direct influence on the moisture variance in the quasi-steady regime. We intend to explore and quantify this link between the initial conditions and the quasi-steady state resulting from cloud organization in order to enable the future development of a parameterization of cloud organization.

Compared to Anurose et al. (2020), we use a more objective definition of the individual regimes. Furthermore, we propose a relatively simple predictor that characterizes the initial moisture profile and exhibits a strong correlation with the moisture variance in the quasi-steady regime. Such a predictor could be used for the estimation of the moisture variance in equilibrium and thus can be useful for the parametrization of cloud organization in shallow convection. In this study, we analyze data from idealized high resolution large-eddy simulations (LES) with the MicroHH LES code for five different initial moisture profiles based on the GEWEX Cloud System Study (GCSS) Rain in Cumulus over the Ocean (RICO) model intercomparison case (Rauber et al., 2007; van Zanten et al., 2011). The initial moisture profiles are modified in the cloud layer and in the free atmosphere (FA).

The remainder of the paper is organized as follows. Section 2 describes the LES model, the model configuration, as well as the methods utilized for the analysis. The results and their interpretation are presented in Section 3. Conclusions and a future outlook are presented in Section 4.

2. Model and Methodology

2.1. Numerical Model

The numerical model used in this study is the three-dimensional fluid dynamics code MicroHH (van Heerwaarden, van Stratum, & Heus, 2017; van Heerwaarden, van Stratum, Heus, Gibbs, et al., 2017). It was primary developed for direct numerical simulation, but includes also a LES configuration. The model solves the filtered Navier-Stokes equations under the anelastic approximation on a staggered Arakawa C-grid with
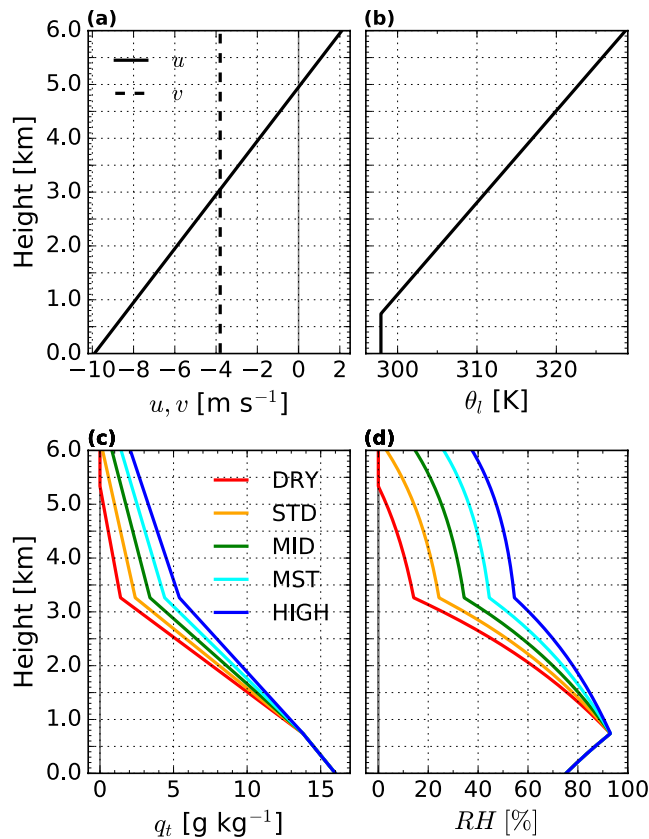
Figure 1. The initial profiles of (a) the wind components, u and v, (b) the liquid water potential temperature, θ_l, (c) the total moisture content, q_t, and (d) the relative humidity, RH. Note that only the total moisture content differs between the cases. STD, standard case.

a fully conservative second-order finite difference scheme in space, and a third-order Runge-Kutta scheme in time. The prognostic variables are fluctuations of density, pressure, and temperature. Moist thermodynamics are used in all our experiments. The subgrid-scale fluxes are modeled by the Smagorinsky-Lilly scheme (Lilly, 1996). Cloud microphysical processes are calculated based on the two-moment warm rain scheme of Seifert and Beheng (2001) with a constant cloud-droplet concentration of 70 cm^{-2}. The top and lower boundaries are defined by a free slip and no slip condition, respectively. The surface fluxes are calculated according to the Monin-Obukhov similarity theory approach using bulk aerodynamic equations. The lateral boundary conditions are periodic. The gravity waves are damped by a buffer layer, which starts at 5.5 km height.

2.2. Experimental Setup

The experimental setup follows the configuration used in the GCSS RICO model intercomparison case (Rauber et al., 2007; van Zanten et al., 2011), which is a composite case based on several days during an undisturbed period in the RICO campaign. It is an exemplary representation of trade-wind shallow cumulus clouds as they develop in marine sub-tropical regions under large-scale subsidence. A set of five simulations are carried out with five different initial conditions for moisture. Remaining initial conditions, boundary conditions, and large-scale forcings are identical for all five simulations and follow the GCSS configuration.

The vertical moisture profiles vary in the cloud layer and the FA, as can be seen in Figure 1. The experiment defined as the standard case (STD) uses the GCSS configuration, while the others are simulations with different vertical moisture contents. The moisture content increases from the driest case, DRY, through STD, MID, MST, and HIGH. This is achieved via modification of the moisture slope in the cloud layer and the FA with the aim of changing the initial bulk vertical gradient of moisture while staying relatively close to the standard RICO case.

All simulations are performed on a $50 \times 50 \times 6$ km grid with an isotropic grid spacing of 25 m. The simulation time is 60 h with an adaptive time step of the order of 1 s. The time resolution of the model outputs is 1 min. Large-scale advective tendencies for temperature and moisture are prescribed, together with the effects of radiation and subsidence. The geostrophic wind field is specified so that the overall setup corresponds to the characteristic height-dependent wind rotation in the trade-wind region within a weakly stratified atmosphere. The surface temperature is fixed (299.8 K) for the duration of the simulation. The surface momentum and thermodynamic fluxes are parameterized using the bulk aerodynamic approach with prescribed exchange coefficients (van Zanten et al., 2011).

2.3. Budget Equation

We want to quantitatively express the cloud organization in precipitating shallow convection in terms of the moisture variance. To understand how cloud organization contributes to the moisture variance, we utilize its domain-averaged budget equation. In accordance with Schemann and Seifert (2017), the domain budget is assumed to be sufficiently closed so that contributions by unresolved subgrid-scale processes can be neglected with the exception of dissipation. Then after assuming incompressibility and horizontal homogeneity, the domain-averaged budget equation for the moisture variance can be written in the following way (Stull, 1988):

$$\frac{\partial \overline{q_t'^2}}{\partial t} = \underbrace{-2\overline{q_t'w'}\frac{\partial \overline{q_t}}{\partial z}}_{\text{I}} - \underbrace{\frac{\partial \overline{w'q_t'^2}}{\partial z}}_{\text{II}} + \underbrace{2\overline{q_t'Q_{q_t}}}_{\text{III}} - \underbrace{2\epsilon_{q_t}^x}_{\text{IV}},$$

(1)

where the over-bar operator, $^-$, denotes horizontal averaging over the domain and $\overline{q_t'^2}$ is the horizontally averaged moisture variance. Term I represents the gradient production term and term II represents the turbulent transport of moisture variance. Term III describes the microphysical sources and sinks of the moisture variance, in which the microphysical tendency Q_{q_t} consists of accretion, autoconversion, and evaporation. Term IV is the subgrid-scale molecular destruction rate. From the results in Anurose et al. (2020), it is clear that the gradient production term I in Equation 1 is the main source term of $\overline{q_t'^2}$ in the RICO case. Hence, we focus in our analysis of the moisture variance on the gradient production term and its components: the vertical moisture flux $\overline{q_t'w'}$ and the vertical moisture gradient $\overline{q_t}z$. Please note that $\overline{q_t'w'}$ is computed without the LES subgrid-scale contribution.

2.4. Data Analysis

2.4.1. Sublayers of the ABL

In order to understand the variability of moisture and through that the cloud organization in the whole vertical column, we will mainly analyze the column-averaged moisture variance $\langle \overline{q_t'^2} \rangle$. The $\langle \rangle$ operator denotes a column-average.

Even when we focus on a column-averaged variable $\langle \overline{q_t'^2} \rangle$, a detailed knowledge of the vertical distribution of the involved processes is still required. Therefore, we follow Anurose et al. (2020) and separate the cloudy trade-wind boundary layer into three sublayers: the sub-cloud layer (SCL), the bulk cloud layer (BCL), and the cloud inversion layer (CIL). The SCL is the layer from the surface up to the cloud base, defined as the altitude where $q_l \geq 10^{-3}$ mg kg^{-1}. For the definition of the BCL, a gradient approach is applied. Here, we define the top of the BCL as the height, where the smoothed q_l reaches its maximum. The local maximum is detected if $q_l \geq 1 \times 10^{-3}$ mg kg^{-1}, and the gradients above and below this level do not exceed a threshold of 4×10^{-6} mg kg^{-1} m^{-1}. The CIL extends from this peak of q_l to the altitude where q_l becomes zero. For detailed information about the spatial and temporal variability of the three sublayers and cloud depth, see the Supporting Information (Figures S1, S2 and S3).

2.4.2. The Three Regimes

As mentioned in the introduction, the temporal evolution of $\langle \overline{q_t'^2} \rangle$ can be divided into three regimes: (a) initial regime, (b) transition regime, and (c) quasi-steady regime. The three regimes are separated by two points in time. The first point is the end of the initial regime, when $\langle \overline{q_t'^2} \rangle$ starts to grow rapidly because of the onset of precipitating convection and the associated cloud organization. The second point is the start of the quasi-steady regime, when the equilibrium condition for the moisture variance is reached. In our study, we declare the former condition to be met if sufficient moisture has accumulated in the ABL and rainwater is formed with a column-integrated rainwater path (RWP) of 8 g m^{-2}. For the equilibrium condition, we consider a case-specific definition, because the amount of generated moisture variance in the transition regime varies between the different initial conditions. The beginning of the quasi-steady regime, t_{qstdy}, is defined for each case with the help of the 5 h moving average of $\langle \overline{q_t'^2} \rangle$, $\langle \overline{q_t'^2} \rangle_{MA}$. Then t_{qstdy} is based on the linear trend of $\langle \overline{q_t'^2} \rangle_{MA}$ estimated via the least square method over a 1 h period. The quasi-steady regime starts when the linear trend falls below 30% of its maximum value, and does not exceed this threshold in the following 5 h.
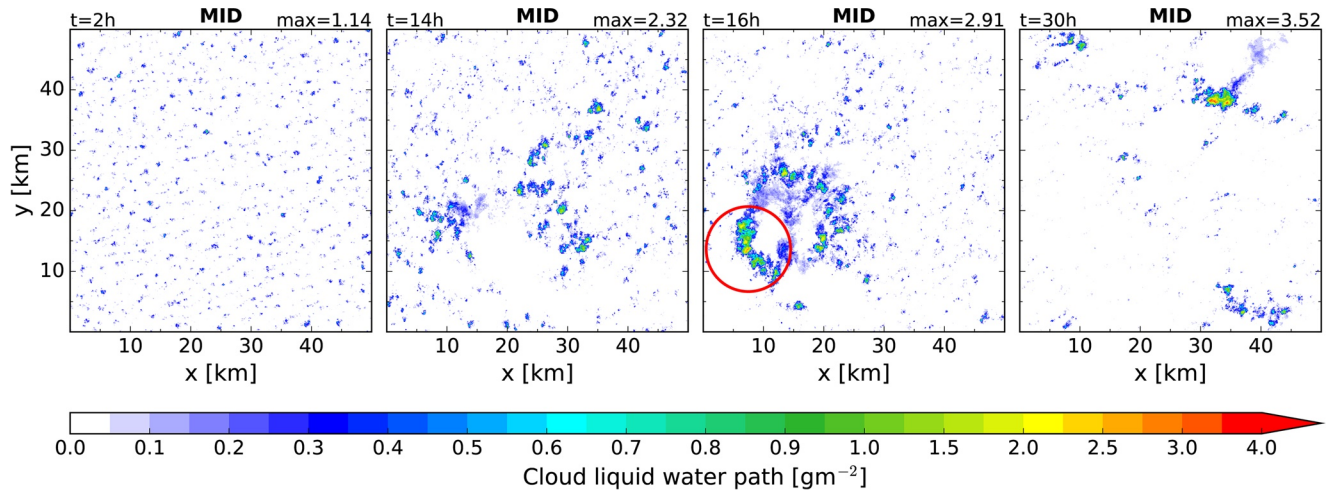
Figure 2. Snapshots of the cloud liquid water path for the MID case after 2, 14, 16, and 30 h of simulation with the respective maximum values. The red circle highlights an arc-shaped mesoscale cloud structure.

2.4.3. Initial State Characteristic

To evaluate the sensitivity of the quasi-steady state $\langle \overline{q_t'^2} \rangle$ with respect to the selected initial moisture profile we need a suitable diagnostic that characterizes the initial state. Since the moisture gradient is an important part of the gradient production term for moisture variance, we propose to use the moisture gradient as a diagnostic of the initial state. We will show that the gradient between the average total moisture content in the SCL and the FA is a useful variable for this purpose:

$$\Delta \overline{q_t} = \frac{\overline{q_t}^{SCL} - \overline{q_t}^{FA}}{z^{FA} - z^{SCL}} \tag{2}$$

On the basis of the selected vertical moisture profiles in Figure 1, $\overline{q_t}^{SCL}$ is the average moisture content in the SCL ranging from the lowest model level at $z = 12.5m$ up to $z = 737.5m$ and $\overline{q_t}^{FA}$ is the average moisture content in the FA ranging from $z = 3262.5m$ up to a height of $z = 5500m$. It should be mentioned that these heights are only postulated for the large-scale setup used in this study.

3. Results

3.1. Temporal Evolution

The evolution of the column-averaged moisture variance, $\langle \overline{q_t'^2} \rangle$, generated during cloud organization in precipitating shallow convection, is investigated here in detail. We focus particularly on the sensitivity of moisture variance on the moisture profile. The impact of precipitation on the evolution of the cloud field is documented using different cloud diagnostics: the domain-averaged RWP, cloud liquid water path (CLWP), and cloud cover (CC). Additionally, the level of cloud organization is subjectively assessed via the spatial distribution of the cloud CLWP. In the following evaluation, we use the MID case to demonstrate typical behavior for all cases. We highlight the differences among the cases, if they are significant.

3.1.1. Initial Regime

Figure 2 shows the evolution of the simulated cloud field for the MID case. Shallow cumulus clouds start to form after approximately 2 h of model spin-up. At this time, there exist many clouds with a low CLWP of less than $1.15 \, g \, m^{-2}$, which are surrounded by larger cloud free areas. Statistically, the cloud distribution in the initial regime is similar for all cases. They differ only in the maximum value of the CLWP, which is due to differences in the moisture content in the cloud layer (see Figure 3). All cases have similar vertical
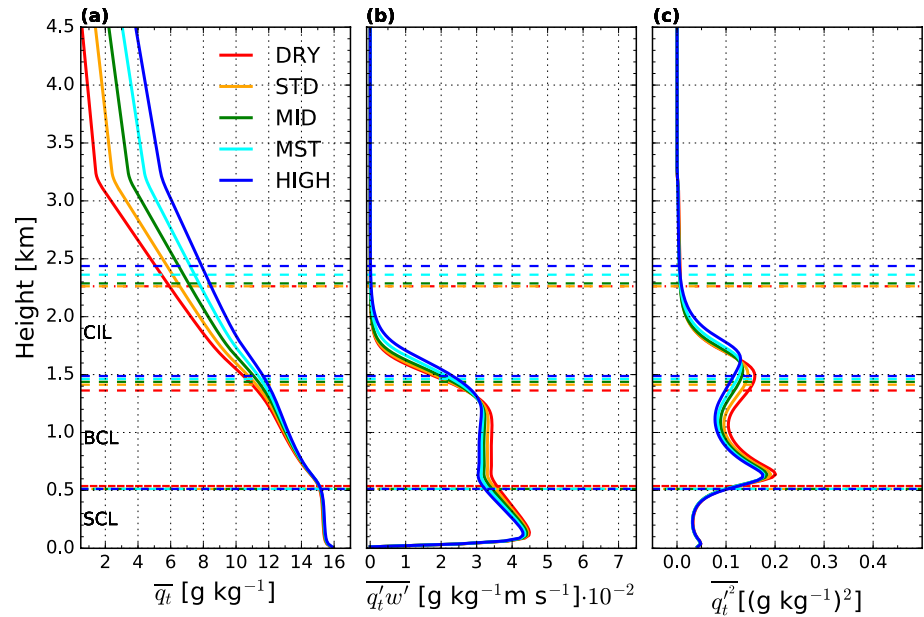
Figure 3. The domain-averaged vertical profiles of (a) the total moisture content, (b) the total moisture flux, and (c) the moisture variance averaged over 5 h starting from the second hour of the simulation. The respective heights of the sub-cloud layer (SCL), bulk cloud layer (BCL), and cloud inversion layer (CIL) are indicated by the horizontal dashed lines. STD, standard case.

profiles of the moisture fluxes and the moisture variances. The moisture variance has the largest values near the SCL and the CIL.

Precipitation is important for the further structural development of the shallow cumulus cloud field. As explained in the introduction, the evaporation of precipitation in the SCL leads to the formation of cold pools, which trigger additional convection. The result is an aggregation of the initially randomly distributed shallow cumulus clouds into larger clusters or mesoscale arcs. This process can be associated with a substantial increase of $\overline{q_t'^2}$ as has been shown by several studies (Anurose et al., 2020; Bretherton & Blossey, 2017; Griffin & Larson, 2016; Schemann & Seifert, 2017; Seifert & Heus, 2013). Figure 4 shows the time series of $\overline{q_t'^2}$ for all cases.

As explained in Section 2.3, the gradient production term in Equation 1 plays a dominant role in the generation of the moisture variance $\overline{q_t'^2}$ in the ABL. The gradient production term is by definition influenced by the product of the moisture flux and the moisture gradient (see Figure 3 for typical profiles). Hence, both factors need to be large enough in order to have a strong enough gradient production term. However, such a situation is not common. On the one hand, the vertical moisture flux, if present, reduces the vertical moisture gradient. On the other hand, a sharp gradient of moisture is typically an indication of stable stratification, which inhibits the moisture flux (Anurose et al., 2020; Ďurán et al., 2018). Consequently, a large gradient production term is usually achieved only temporary, for example, during the local penetration of stable stratification by active convection. In our case, only precipitating convection is strong enough to penetrate the stable layer capping the ABL. Thus, the gradient production term is relatively large only for a limited time until the local moisture gradient is reduced and a new moisture gradient forms above the former one.

Since most moisture variance is generated via the gradient production term near the BCL-CIL interface, the maximum of the domain-averaged moisture gradient and moisture flux in levels near this interface (± 125 m) is shown in Figure 5. It can be seen that during the initial regime, a combination of a persistent surface moisture flux and a minimal exchange with the CIL results in a continual growth of the negative vertical moisture gradient at the BCL-CIL interface. After some time, the continuous accumulation of moisture results in the formation of rainwater. This process is accompanied with latent heat release, which increases
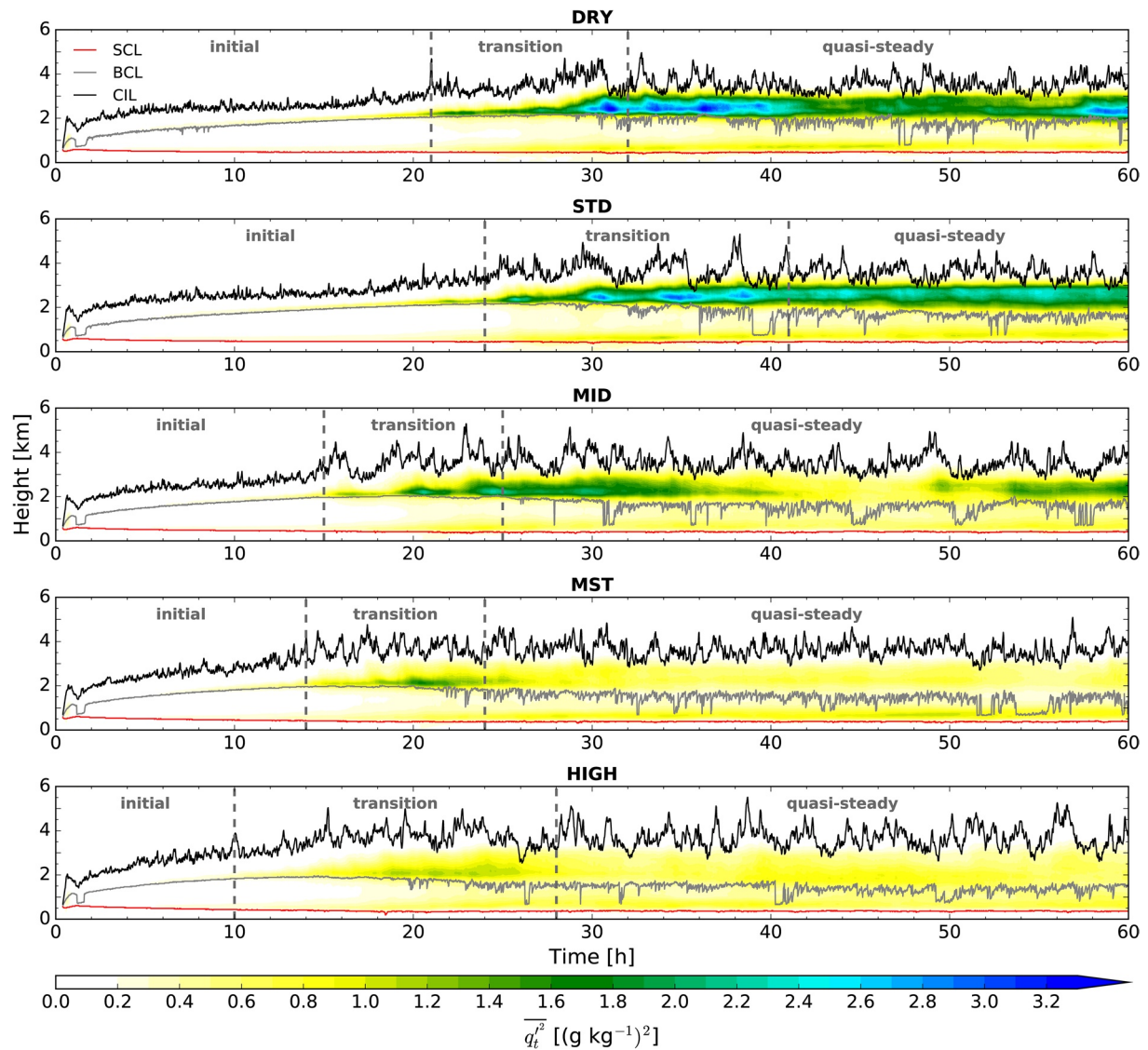
Figure 4. Time-height plot of the moisture variance $\overline{q_t'^2}$ (shaded). The lines denote the top of the sub-cloud layer (SCL) (red), the bulk cloud layer (BCL) (gray), and the cloud inversion layer (CIL) (black), respectively. The gray dashed vertical lines delineate the initial, transition, and quasi-steady regime. STD, standard case.

the buoyancy of the air in the BCL. Even at this stage, the stable layer above the BCL-CIL is only seldomly penetrated, thus the moisture gradient still increases, and the moisture flux across the interface remains relatively small. Consequently, the gradient production term grows only thanks to the increase in the moisture gradient. This means a steady, but rather weak increase of the column-averaged moisture variance, as can be seen for the MID case in Figure 5c. Therefore, $\langle \overline{q_t'^2} \rangle$ reaches the threshold value of 0.1 $g^2\,kg^{-2}$ only after a rather long 15 h period in the initial regime.

3.1.2. Transition Regime

After longer integration, the accumulation of moisture in the BCL, and the accompanied latent heat release is large enough to cause active convection that penetrates the BCL-CIL interface. In Section 2.4.2, we defined this time as the beginning of the transition regime at which the RWP first reaches a threshold of 8 g m^{-2}. The first column of Table 1 shows the start of the transition regime (rounded to the nearest hour) for the different cases. The transition regime is reached earliest for the HIGH case after 10h of simulation
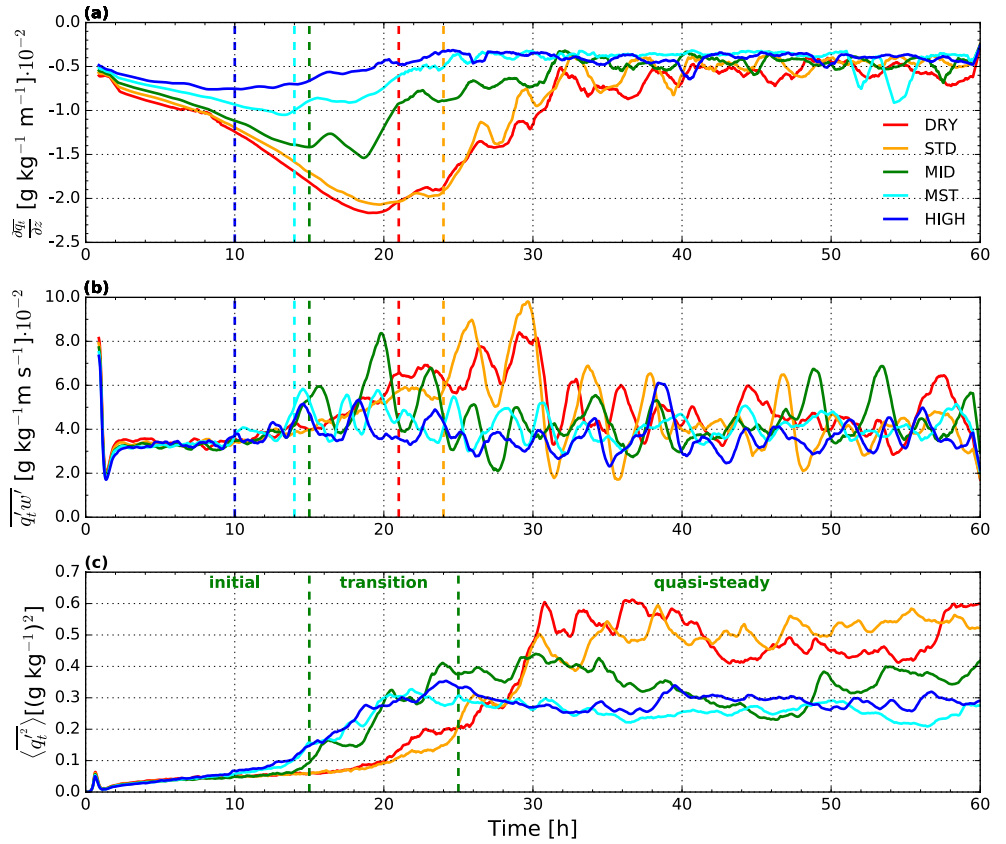
Figure 5. Time series of (a) the vertical maximum of the domain-averaged moisture gradient and (b) the moisture flux near the bulk cloud layer-cloud inversion layer interface. The vertical maximum was computed from 1 h moving averages. Time series of the column-averaged moisture variance, $\langle \overline{q_t'^2} \rangle$, are shown in (c). The colored vertical dashed lines in (a) and (b) mark the beginning of the transition regime for each case. The dark green vertical dashed lines in (c) mark the beginning of the transition and quasi-steady regime for the MID case. STD, standard case.

and latest for the STD case at $t = 24$h. A general temporal shift from moist to dry cases can be inferred for the beginning of the transition regime. Obviously, the temporal shift is related to the earlier onset of precipitation for the moister cases (see Figure 6).

The transition regime is characterized by the transformation of individually distributed clouds into organized mesoscale cloud structures. As explained in Section 3.1.1, this process is accompanied by active

Table 1
Start and End Times of the Transition Regime for All Five Cases, and the Corresponding Column-Averaged Moisture Variance $\langle \overline{q_t'^2} \rangle$

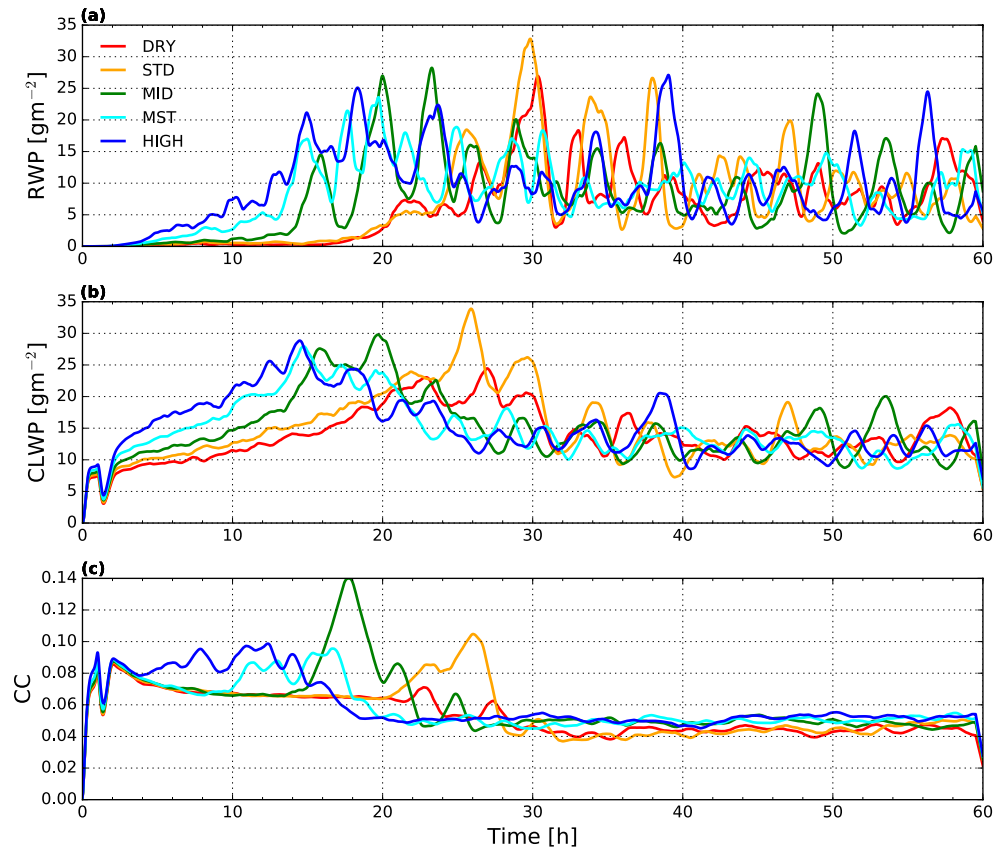| | Regimes | | $\langle \overline{q_t'^2} \rangle$ | |
Cases	Transition (h)	Quasi-steady (h)	Start (g^2 kg^{-2})	End (g^2 kg^{-2})
DRY	21	32	0.13	0.52
STD	24	41	0.15	0.49
MID	15	25	0.09	0.38
MST	14	24	0.10	0.28
HIGH	10	28	0.07	0.29

Abbreviation: STD, standard case.

Figure 6. Time series of the domain-averaged 1 h moving average of (a) the rainwater path (RWP), (b) the cloud liquid water path (CLWP), and (c) the cloud cover (CC). STD, standard case.

convection that significantly contributes to an increase of the moisture variance (see Figure 4). Convection transports moisture into the CIL across the zone with a pronounced moisture gradient at the BCL-CIL interface. This leads to a greater vertical extent of the CIL (see Figure 7). An example for mesoscale organization is the evolution of the MID case in Figure 5b, which shows a peak of approximately 0.06 g kg^{-1} m s^{-1} at $t = 16$h. At this time, an arc-shaped mesoscale cloud structure can be observed in Figure 2, highlighted by the red circle. The mesoscale organization is probably connected to the formation of a cold pool, which can be detected as a large cloud free area in positive x and y direction relative to the location of the maximum CLWP.

The transition regime is also characterized by short-term periods of increased and decreased convective activity. The transition regime of the MID case exhibits three such major peaks of $\overline{(q_t' w')}$ at approximately $t = 16$h, $t = 20$h and $t = 23$h. During these periods, the moisture gradient is reduced and a new weaker moisture gradient is formed above the former one. This can be deduced from Figure 5a, which shows a reduction of the moisture gradient at the respective times. Between these reductions of the moisture gradient, short-term increases of the maximum $\overline{q_t}z$ can be detected. These are related to phases of lower convective activity, in which the moisture accumulation, owing to the surface moisture flux, dominates over the moisture transport across the BCL-CIL interface. This is most obvious at approximately $t = 19$h. At this time, the MID case reaches a secondary maximum in $\overline{q_t}z$. In cases of a large initial moisture content, like for MST and for HIGH, cycles in convective activity are more difficult to detect. This is due to generally much smaller magnitudes of the maximum in $\overline{q_t}z$ and $\overline{(q_t' w')}$, compared to the drier cases. Concerning the individual experiments, the magnitude of the maximum $\overline{q_t}z$ is the largest for the drier simulations (see Figure 5a). In the long-term, the maximum of $\overline{q_t}z$ decreases during the transition regime for all five simulations.
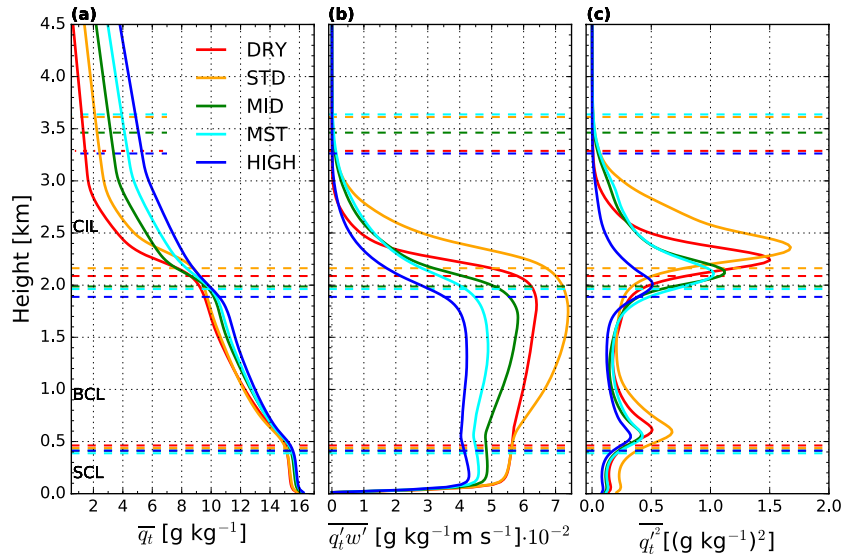
Figure 7. As in Figure 3, but averaged over 5 h starting from the case-specific transition regime. BCL, bulk cloud layer; CIL, cloud inversion layer; SCL, sub-cloud layer; STD, standard case.

The peaks of $\overline{(q_t'w')}$ lead to sharp increases of $\langle \overline{q_t'^2} \rangle$. Therefore, the temporal development of $\langle \overline{q_t'^2} \rangle$ shown in Figure 5c is also subject to cycles on top of a steady increase during the transition regime. For the MID case, an increase of $\langle \overline{q_t'^2} \rangle$ from 0.15 g^2 kg^{-2} to just above 0.3 g^2 kg^{-2} (between approximately 18 and 20 h) coincides with a strong moisture fluxes $\overline{(q_t'w')}$ of slightly more than 0.08 g kg^{-1} m s^{-1} across the BCL-CIL interface.

3.1.3. Quasi-Steady Regime

At the end of the transition regime, the growth of the moisture variance gets weaker. An equilibrium (defined in Section 2.4.2) is then reached in the following quasi-steady regime (see Figure 4), where the individual terms of the $\langle \overline{q_t'^2} \rangle$ budget balance. This is caused mainly by the decrease in the gradient production term, specifically at the BCL-CIL interface. It can be seen in Figure 5 that both factors in the gradient production term, the moisture gradient and the moisture flux, are gradually reduced via the vertical redistribution of moisture in the transition regime. Thus, changes in $\langle \overline{q_t'^2} \rangle$ remain small in the quasi-steady regime, even when $\langle \overline{q_t'^2} \rangle$ oscillates around an equilibrium value as can be seen in Figure 5c. Similar to the transition regime, these oscillations are caused by the life cycle of convection.

The beginning of the quasi-steady regime, rounded to the nearest hour for each case, is shown in the second column of Table 1. It can be seen that the quasi-steady regime starts latest for the STD case ($t = 41$ h) as is the case for the beginning of the quasi-steady regime. The moisture variance, $\langle \overline{q_t'^2} \rangle$, accumulated during the transition regime is generally smaller for moister cases (see Table 1, right column). While in the DRY case, $\langle \overline{q_t'^2} \rangle$ has increased by 0.39 g^2 kg^{-2}, the MST case exhibits only an increase of 0.18 g^2 kg^{-2}.

Typical vertical profiles of the domain-averaged total moisture content, $\overline{q_t}$, moisture flux, $\overline{q_t'w'}$, and moisture variance, $\overline{q_t'^2}$, during the quasi-steady regime are displayed in Figure 8. As expected, most of the moisture variance is found above the BCL-CIL interface with a distinct increase from moist to dry initial conditions.
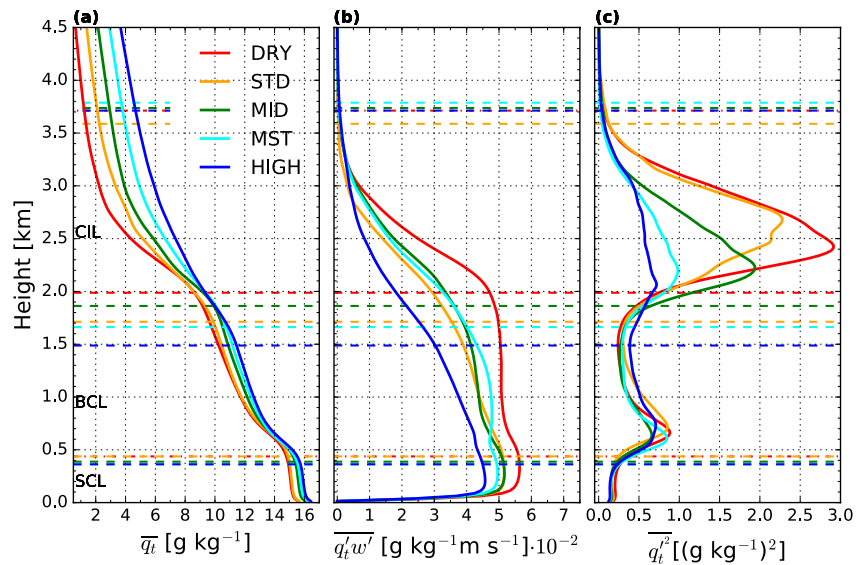
Figure 8. As in Figure 3, but averaged over 5 h starting from the case-specific quasi-steady regime. BCL, bulk cloud layer; CIL, cloud inversion layer; SCL, sub-cloud layer; STD, standard case.

3.2. Correlation Between the Initial State and Quasi-Steady Regime

The objective of this paper is to assess the sensitivity of the moisture variance in the quasi-steady regime to the initial conditions in the RICO case. The vertically integrated quantities, such as the CC and the CLWP in the quasi-steady regime (see Figure 6), seem to be independent of the initial conditions since they look similar for all cases. Their equilibrium values seem to be dictated by the boundary conditions and the atmospheric forcings. In contrast, the vertical profiles of the first order quantities differ in the quasi-steady regime between the cases in a more significant way. As an example, the range of the domain-averaged total

Figure 9. Mean (black) and range (minimum to maximum; orange shading) of the domain-averaged vertical profiles of (a) the total moisture content and (b) the liquid water content averaged over 5 h starting from the case-specific quasi-steady regime. The average heights of the sub-cloud layer (SCL) (red), bulk cloud layer (BCL) (blue), and cloud inversion layer (CIL) (green) are indicated by horizontal lines, including their respective standard deviations. In panel (a), the mean (gray) and range (gray shading) of the corresponding initial profiles are added. FA, free atmosphere.

moisture and liquid water content as a function of height is illustrated in Figure 9. In the profile of the quasi-steady $\overline{q_t}$, it is noticeable that below the BCL-CIL interface the variation is small, but increases within the CIL above 2.2 km and remains relatively large up to the FA. Note that in the lower part of the CIL the spread is reduced in comparison to the initial state.

As we have demonstrated in the previous subsection, the initial conditions have also an impact on vertically averaged moisture variance, which is a vertically averaged second-order quantity. A possible explanation for the influence of initial conditions on the moisture variance is in the deviation of the initial moisture profile from a theoretical equilibrium profile. The initial deviation is transformed during moisture redistribution in the transition regime via the gradient production term into the moisture variance. This explanation is supported by the fact that the vertically averaged moisture variance in the quasi-steady regime is larger for cases with drier conditions, where the deviation from a theoretical equilibrium is larger. Based on this observation, we hypothesize that the quasi-steady column-averaged moisture variance, $\langle q_t'^2 \rangle$, can be inferred from the initial moisture profile for the different cases. In the following, this is corroborated by a correlation analysis between the initial and quasi-steady state. We use the gradient $\Delta \overline{q_t}$ between the average total moisture content in the SCL and the FA to characterize the initial state (see Section 2.4.3), and the temporal average from the first 5 h of the case-specific quasi-steady regime to characterize the equilibrium state.
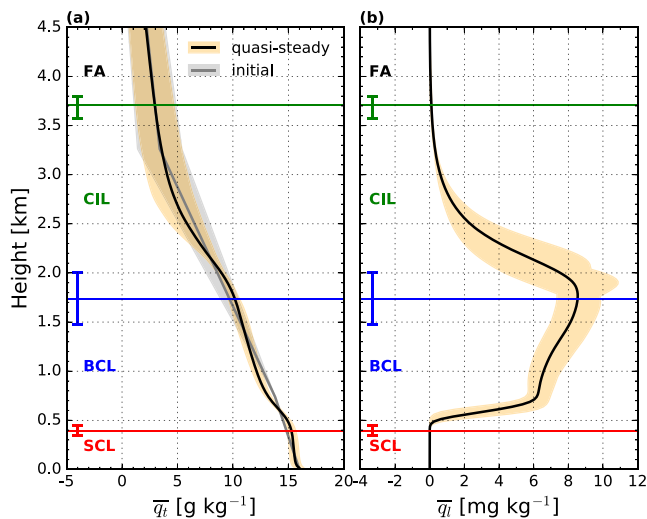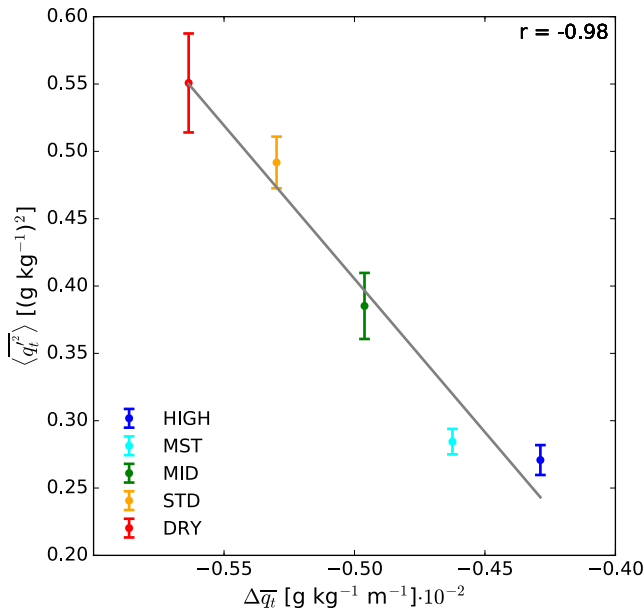
Figure 10. Scatter plot of the case-specific moisture variance $\overline{\langle q_t'^2 \rangle}$ averaged over the first 5 h of the case-specific quasi-steady state versus the respective initial moisture gradient $\Delta \overline{q_t}$. The Pearson correlation coefficient is $r = -0.98$. The error bars indicate the range of $\overline{\langle q_t'^2 \rangle}$ based on the standard deviation of the 1 min values. STD, standard case.

Figure 10 shows the scatter plot of the case-specific quasi-steady column-averaged moisture variance, $\overline{\langle q_t'^2 \rangle}$, versus the case-specific initial moisture gradient, $\Delta \overline{q_t}$, with a linear regression line. There exists a strong correlation between the predictor quantity $\Delta \overline{q_t}$ and the quasi-steady $\overline{\langle q_t'^2 \rangle}$ with a Pearson correlation coefficient of $r = -0.98$. The deviations from the regression line are small. For the present large-scale setup, this result indicates that the prescribed moisture gradient of the initial state, $\Delta \overline{q_t}$, is a suitable predictor to estimate the column-averaged moisture variance, $\overline{\langle q_t'^2 \rangle}$, in the quasi-steady state. This confirms the indications from Anurose et al. (2020) that there exists a relationship between the initial moisture profile and the quasi-steady column-averaged moisture variance. For comparison, there is basically no correlation between cloud depth in the quasi-steady regime and the initial conditions (see Figure S4 in the Supporting Information).

The validity of these results beyond these specific cases and beyond RICO needs to be further investigated. First of all, the quasi-steady moisture variance can be influenced also by boundary conditions and atmospheric forcings, which were kept the same during this study. Also, the initial moisture profile had a similar vertical structure for all cases, and changing the vertical structure could result in a different behavior. Nonetheless, the strong relationship is remarkable, considering the complexity of the involved processes. The strong relationship could be advantageous for the development of a parametrization of cloud organization in precipitating shallow convection, where a bulk moisture gradient could be used as a predictor for shallow convection organization. Estimation of the deviation of the moisture profile from a theoretical equilibrium profile would be even more suitable for this task, but such an estimation is beyond the scope of this paper.

4. Summary and Conclusion

We have investigated the sensitivity of the quasi-steady state of precipitating shallow convection to the initial moisture profile. The focus has been on the sensitivity of the column-averaged moisture variance, $\langle \overline{q_t'^2} \rangle$, because this quantity can be linked to cloud organization.

Five idealized simulations based on the GCSS RICO model intercomparison case were run with the Micro-HH LES model. The five simulations differ only in their initial moisture profile. Cloud organization in the precipitating shallow convection develops in all five cases.

Similarly to Anurose et al. (2020), we divided the cloud field evolution into three regimes: (a) initial regime, (b) transition regime, and (c) quasi-steady regime. The transition regime starts with the onset of precipitation, specifically when the column-integrated RWP reaches a predefined threshold value. In the transition regime, precipitating active convection intensifies. The intensification is linked to the mesoscale organization of the cloud field. The transition regime is characterized by active convection, where the penetration of the convection across the top of the cloud layer leads to an increase of the moisture variance. This can be attributed to an increase in the gradient production term, which is large, because convection transports moisture across a region with a strong moisture gradient. This process continues until the generation of moisture variance is reduced due to the redistribution of moisture and a quasi-steady regime is reached. Comparing the simulations, an increase of the accumulation of $\langle \overline{q_t'^2} \rangle$ in the transition regime from moist to dry cases is observed. The onset of the transition regime and the onset of the quasi-steady regime differs between the cases. Generally, both regimes start sooner for moister cases, and are delayed for drier cases.

It is found that the initial moisture profile influences the quasi-steady moisture variance. For the selected large-scale setup, the initial moisture gradient between the average SCL and the FA, $\Delta\overline{q_t}$, seems to be a suitable predictor to quantify the quasi-steady moisture variance $\langle \overline{q_t'^2} \rangle$. It has been shown that there exists a strong linear relationship between the initial moisture gradient $\Delta\overline{q_t}$ and quasi-steady moisture variance $\langle \overline{q_t'^2} \rangle$ with a Pearson correlation coefficient of $r = -0.98$. This finding suggests that the moisture gradient or its deviation from an equilibrium value is an important factor that influences the quasi-steady moisture variance and can thus be used to estimate the quasi-steady state of the precipitating shallow cumulus cloud field. The result is remarkable with regard to the complexity of the processes, which accompany the cloud organization in cases with precipitating shallow convection. The quantification of the link between initial conditions and quasi-steady state is an important step towards a subgrid scale parametrization of cloud organization, in which the quasi-steady state of cloud organization can be used as a basis. The development of a subgrid scale parametrization of cloud organization is beyond the scope of the paper and is left for further studies.

The result of this study is only valid for the GCSS RICO model intercomparison case. A general parametrization should provide an acceptable result for a variety of different conditions. Future studies should investigate whether other important factors beside the initial moisture gradient, or the deviation of the moisture profile from an equilibrium state respectively, influence the quasi-steady moisture variance. For this purpose, further sensitivity studies should be performed, which should include a variation of initial conditions, modification of boundary conditions and atmospheric forcings.

Data Availability Statement

The data for this study were generated with the LES model MicroHH, which is openly available in Zenodo at https://zenodo.org/record/822842 (van Heerwaarden, van Stratum, & Heus, 2017; van Heerwaarden, van Stratum, Heus, Gibbs, et al., 2017). The configuration files and output statistics of the five simulations (DRY, STD, MID, MST, and HIGH) are openly available in Zenodo at https://zenodo.org/record/4621201 (Thomas et al., 2021). All figures were generated with the Python matplotlib package (Hunter, 2007).

References

Anurose, T. J., Bašták Ďurán, I., Schmidli, J., & Seifert, A. (2020). Understanding the moisture variance in precipitating shallow cumulus convection. *Journal of Geophysical Research: Atmospheres*, *125*(1). https://doi.org/10.1029/2019JD031178

Bony, S., & Dufresne, J.-L. (2005). Marine boundary layer clouds at the heart of tropical cloud feedback uncertainties in climate models. *Geophysical Research Letters*, *32*(20). https://doi.org/10.1029/2005GL023851

Bony, S., Stevens, B., Frierson, D. M. W., Jakob, C., Kageyama, M., Pincus, R., et al. (2015). Clouds, circulation and climate sensitivity. *Nature Geoscience*, *8*, 261–268. https://doi.org/10.1038/ngeo2398

Bretherton, C. S., & Blossey, P. N. (2017). Understanding mesoscale aggregation of shallow cumulus convection using large-eddy simulation. *Journal of Advances in Modeling Earth Systems*, *9*(8), 2798–2821. https://doi.org/10.1002/2017MS000981

Ďurán, I. B., Geleyn, J.-F., Váňa, F., Schmidli, J., & Brožková, R. (2018). A turbulence scheme with two prognostic turbulence energies. *Journal of the Atmospheric Sciences*, *75*(10), 3381–3402. https://doi.org/10.1175/JAS-D-18-0026.1

Fritsch, J., & Chappell, C. F. (1980). Numerical prediction of convectively driven mesoscale pressure systems. Part I: Convective parameterization. *Journal of the Atmospheric Sciences*, *37*(8), 1722–1733.

Griffin, B. M., & Larson, V. E. (2016). Parameterizing microphysical effects on variances and covariances of moisture and heat content using a multivariate probability density function: A study with clubb (tag MVCS). *Geoscientific Model Development*, *9*, 4273–4295. https://doi.org/10.5194/gmd-9-4273-2016

Hunter, J. D. (2007). Matplotlib: A 2D graphics environment. *Computing in Science & Engineering*, *9*(3), 90–95. https://doi.org/10.1109/MCSE.2007.55

Lilly, D. K. (1996). A comparison of incompressible, anelastic and boussinesq dynamics. *Atmospheric Research*, *40*(2), 143–151. https://doi.org/10.1016/0169-8095(95)00031-3

Nair, U. S., Weger, R. C., Kuo, K. S., & Welch, R. M. (1998). Clustering, randomness, and regularity in cloud fields: 5. The nature of regular cumulus cloud fields. *Journal of Geophysical Research*, *103*(D10), 11163–11380. https://doi.org/10.1029/98JD00088

Rauber, R. M., Stevens, B., Ochs, H. T., Knight, C., Albrecht, B. A., Blyth, A. M., et al. (2007). Rain in shallow cumulus over the ocean: The rico campaign. *Bulletin of the American Meteorological Society*, *88*(12), 1912–1928. https://doi.org/10.1175/BAMS-88-12-1912

Schemann, V., & Seifert, A. (2017). A budget analysis of the variances of temperature and moisture in precipitating shallow cumulus convection. *Boundary-Layer Meteorology*, *163*(3), 357–373. https://doi.org/10.1007/s10546-016-0230-1

Seifert, A., & Beheng, K. D. (2001). A double-moment parameterization for simulating autoconversion, accretion and selfcollection. *Atmospheric Research*, *59–60*, 265–281. https://doi.org/10.1016/s0169-8095(01)00126-0

Seifert, A., & Heus, T. (2013). Large-eddy simulation of organized precipitating trade wind cumulus clouds. *Atmospheric Chemistry and Physics Discussions*, *13*, 1855–1889. https://doi.org/10.5194/acpd-13-1855-2013

Sherwood, S., Bony, S., & Dufresne, J. (2014). Spread in model climate sensitivity traced to atmospheric convective mixing. *Nature*, *505*, 37–42. https://doi.org/10.1038/nature12829

Snodgrass, E. R., Di Girolamo, L., & Rauber, R. M. (2009). Precipitation characteristics of trade wind clouds during rico derived from radar, satellite, and aircraft measurements. *Journal of Applied Meteorology and Climatology*, *48*(3), 464–483. https://doi.org/10.1175/2008JAMC1946.1

Stull, R. B. (1988). *An introduction to boundary layer meteorology*. Kluwer Academic Publishers. https://doi.org/10.1007/978-94-009-3027-8

Thomas, M. L., Bastak Duran, I., & Schmidli, J. (2021). *Data for the publication "Towards parametrization of precipitating shallow cumulus cloud organization via moisture variance" [Data set]*. Zenodo. https://doi.org/10.5281/zenodo.4621201

Tiedtke, M. (1989). A comprehensive mass flux scheme for cumulus parameterization in large-scale models. *Monthly Weather Review*, *117*(8), 1779–1800. https://doi.org/10.1175/1520-0493(1989)117<1779:acmfsf>2.0.co;2

Tobin, I., Bony, S., & Roca, R. (2012). Observational evidence for relationships between the degree of aggregation of deep convection, water vapor, surface fluxes, and radiation. *Journal of Climate*, *25*(20), 6885–6904. https://doi.org/10.1175/JCLI-D-11-00258.1

Tompkins, A. M., & Semie, A. G. (2017). Organization of tropical convection in low vertical wind shears: Role of updraft entrainment. *Journal of Advances in Modeling Earth Systems*, *9*(2), 1046–1068. https://doi.org/10.1002/2016MS000802

van Heerwaarden, C. C., van Stratum, B. J. H., & Heus, T. (2017). *microhh/microhh: 1.0.0 (Zenodo; Version 1.0.0) [Data set]*. Zenodo. https://doi.org/10.5281/zenodo.822842

van Heerwaarden, C. C., van Stratum, B. J. H., Heus, T., Gibbs, J. A., Fedorovich, E., & Mellado, J. P. (2017). Microhh 1.0: A computational fluid dynamics code for direct numerical simulation and large-eddy simulation of atmospheric boundary layer flows. *Geoscientific Model Development*, *10*(8), 3145–3165. https://doi.org/10.5194/gmd-10-3145-2017

van Zanten, M. C., Stevens, B., Nuijens, L., Siebesma, A. P., Ackerman, A. S., Burnet, F., et al. (2011). Controls on precipitation and cloudiness in simulations of trade-wind cumulus as observed during rico. *Journal of Advances in Modeling Earth Systems*, *3*(2). https://doi.org/10.1029/2011MS000056

Vial, J., Bony, S., Stevens, B., & Vogel, R. (2017). Mechanisms and model diversity of trade-wind shallow cumulus cloud feedbacks: A review. *Surveys in Geophysics*, *38*, 1331–1353. https://doi.org/10.1007/s10712-017-9418-2

Webb, M. J., Senior, C. A., Sexton, D. M. H., Ingram, W. J., Williams, K. D., Ringer, M. A., et al. (2006). On the contribution of local feedback mechanisms to the range of climate sensitivity in two GCM ensembles. *Climate Dynamics*, *27*(1), 17–38. https://doi.org/10.1007/s00382-006-0111-2

Zuidema, P., Li, Z., Hill, R. J., Bariteau, L., Rilling, B., Fairall, C., et al. (2012). On trade wind cumulus cold pools. *Journal of the Atmospheric Sciences*, *69*(1), 258–280. https://doi.org/10.1175/JAS-D-11-0143.1